Operational modal analysis of an end-supported pontoon bridge

Knut Andreas Kvåle[a,*], Ole Øiseth[a], Anders Rönnquist[a]

[a]*Department of Structural Engineering, Faculty of Engineering Science and Technology, NTNU, Norwegian University of Science and Technology, Trondheim, Norway*

Abstract

A comprehensive monitoring system is installed and currently in operation on the Bergsøysund Bridge, an end-supported floating pontoon bridge, collecting data on accelerations, displacements, waves, and wind. Using covariance-driven stochastic subspace identification (Cov-SSI), data-driven stochastic subspace identification, and frequency domain decomposition, the modal parameters of the structure are estimated to investigate its dynamic behaviour. Aspects regarding the selection of good parameters for the Cov-SSI analyses are highlighted, and the clarifying effect of applying stabilization criteria on multiple orders of output is discussed. The effects of the significant wave height on the modal parameters are investigated based on an automatic selection of stable poles from stabilization plots produced by the Cov-SSI method.

Keywords: Bergsøysund Bridge, floating bridge, stochastic subspace identification, high damping

1. Introduction

Floating bridges of various designs have existed for approximately four millennia, according to [1]. However, only in recent decades have such bridges been used in modern infrastructure applications. More crossings may potentially take advantage of floating bridges.

In an international context, the continuous pontoon girder is by far the most common type of floating bridge. Such bridges are generally side supported by anchoring to the seabed, which drastically reduces their flexibility. For some crossings, bridges based on continuous pontoon girders or anchoring are not feasible or beneficial. The crossings planned for the ferry-free Coastal Highway E39, located on the northwestern coast of Norway, are examples of such crossings. The deep fjords make side anchoring to the seabed practically impossible. Furthermore, the requirement that ships should be able to pass through makes a discretely distributed pontoon solution more obvious. Worldwide, only two long-span end-supported floating bridges exist: the Bergsøysund Bridge and the Nordhordland Bridge. Both of these bridges are located on the western coast of Norway, and both rely on discretely distributed pontoons.

The traditional method for dynamic testing is based on estimating the frequency response function matrix, which requires monitoring of both the force and the response quantities. Structures under operation are, however, more commonly studied based on ambient vibrations alone, referred to as operational modal analysis (OMA) or output-only system identification. Since the crude, yet effective, peak-picking study performed on the Golden Gate Bridge by McLamore et al. [2], the research field concerning the OMA of civil structures has experienced significant development. The number of available methods for OMA is continuously increasing, with the acronyms FDD, SSI, ARMA, SOBI and NExT representing some of the most well-known methods. In the works by [3–9], system identification techniques are applied on civil structures, and the performances of the methods are compared. Generally, OMA methods are applied to lightly damped structures. When system identification is to be attempted on a floating bridge, which due to the fluid-structure interaction observes high damping levels, the following question emerges: are the modal analysis methods suitable for a floating bridge?

Answering the above question is the main objective of this paper. Using a state-of-the-art measurement system, the dynamic behaviour of the Bergsøysund Bridge is studied. Both environmental actions, in terms of wind and wave excitation, and global response, in terms of accelerations and displacements, are recorded, and their relationship is investigated. In this regard, the effects of wave and wind conditions on modal parameters are of particular interest. Temperature effects are considered to be beyond the scope of the current paper. The effect of changing temperature has been thoroughly investigated in the literature [6, 10, 11].

Modal identification using covariance-driven stochastic subspace identification (Cov-SSI) on recordings from the Bergsøysund Bridge was also the topic of the conference paper by Kvåle et al. [12]. It was concluded that the identified parameters, corresponding to the lowest modes of the structure, were in decent agreement with the initial numerical predictions of frequency and damping and below satisfactory for mode shapes. The sensitivity of the input parameters to the results, particularly the number of time lags, was very large, and considerable tweaking of the selected values was required. This situation is also known and well reported in the literature, see e.g., [11, 13].

The current study addresses many of the above highlighted issues and is also far more extensive than the mentioned con-

*Corresponding author

ference paper. Furthermore, this study relies on an extended monitoring system, including environmental monitoring. The stabilization criterion is required to be fulfilled for multiple preceding poles to clarify the stabilization plots such that the selection of stable and physical poles is more robust. By automating the selection of modal parameters, the effects of environmental parameters on the modal quantities are studied based on a large pool of recordings.

2. Theoretical outline

2.1. Numerical prediction of modal parameters

For comparison with the predicted modal quantities of the floating bridge, some operations on the system model matrices are needed. The mathematical and numerical model is identical to the one presented in Kvåle et al. [14]. For the convenience of the reader, the most important details are repeated in the following. The goal is to establish a frequency-domain equation of motion to obtain an easily solvable eigenvalue problem. The starting point is the time-domain generic equation of motion, written as follows within the framework of the finite element method (FEM):

$$[M_s]\{\ddot{u}(t)\} + [C_s]\{\dot{u}(t)\} + [K_s]\{u(t)\} = \{p_h(t)\} \tag{1}$$

Here, t represents the time; $[M_s]$, $[C_s]$, and $[K_s]$ are the structural mass, damping and stiffness matrices, respectively; $\{u(t)\}$ is the displacement vector; and $\{p_h(t)\}$ is the total hydrodynamic action, which includes both wave excitation and fluid-structure interaction. The fluid-structure interaction can be treated as frequency-dependent contributions to the system mass and damping and as a constant contribution to the system stiffness. This treatment results in the following equation of motion, represented in a hybrid frequency-time domain:

$$[M(\omega)]\{\ddot{u}(t)\} + [C(\omega)]\{\dot{u}(t)\} + [K]\{u(t)\} = \{p(t)\} \tag{2}$$

Here, the total system matrices, including the fluid-structure interaction contributions, namely, $[M(\omega)]$, $[C(\omega)]$, and $[K]$, are used. The wave excitation vector is denoted as $\{p(t)\}$. From this, the following complex eigenvalue problem is established:

$$\left(\lambda^2[M(\omega)] + \lambda[C(\omega)] + [K]\right)\{u\} = \{0\} \tag{3}$$

where the eigenvalue λ is introduced. The general complex eigenvalue problem is typically solved using a state-space formulation, as in this work. Clearly, cf. Equation 3, the eigenvalue problem is frequency dependent. To accommodate this, an iterative algorithm, represented by the pseudo-code in Table 1, is used.

Note that the estimated numerical solutions to the eigenvalue problem presented in [14] have been re-estimated due to a model update in [15]. The latter estimates are used as a reference in this paper.

Table 1: Pseudo-code of the iterative algorithm used to solve the eigenvalue problem [14].

```
INPUT N, tolerance
FOR n = 1 to 2N
    ω = 0
    Δ = tolerance + 1
    WHILE Δ > tolerance
        Solve eigenvalue problem for chosen ω ⇒ λ_r and {q_r}
        Sort λ_r, and correspondingly sort {q_r}
        ω_0 = ω
        ω = |λ_n|   (n = r)
        Δ = |ω_0 − ω|
    END
    Store eigenvalue λ_n = λ_r and eigenvector {q_n} = {q_r}
END
```

2.2. Modal identification

2.2.1. Frequency domain decomposition

The simple and effective improvement of the peak-picking method, based on singular value decomposition (SVD), was presented, in its current form, by Brincker et al. [16, 17]: the frequency domain decomposition (FDD). To some extent, this can remedy difficulties from closely spaced modes but stays true to the simple and tangible interpretation that follows the peak-picking method. This makes it an ideal method to supplement more sophisticated methods that often suffer from less graspable interpretations.

2.2.2. Covariance-driven stochastic subspace identification

The stochastic subspace identification methods are highly sophisticated techniques and are considered to be among the most robust and accurate methods available [3, 4]. The Cov-SSI method enables the identification of a stochastic state-space model based on response measurements only. The following presentation, which summarizes the main elements of the algorithm, is based on Hermans and van Der Auweraer [18].

First, assume the following stochastic and discrete state-space model representing the considered dynamical system:

$$\{z_{k+1}\} = [A]\{z_k\} + \{w_k\} \tag{4}$$

$$\{y_k\} = [C]\{z_k\} + \{v_k\} \tag{5}$$

where $\{z_k\}$ and $\{y_k\}$ are the state vector and output vector, respectively, and $\{w_k\}$ and $\{v_k\}$ are noise terms. The sub-indices correspond to discrete time sample numbering, related to the time through $t = (k-1)f_s^{-1}$, where f_s is the sampling frequency. Furthermore, $[A]$ is the state matrix and $[C]$ is the output matrix.

The recorded data are arranged in a matrix $[Y]$ as follows:

$$[Y] = \begin{bmatrix} \{y_1\}^T \\ \{y_2\}^T \\ \vdots \\ \{y_N\}^T \end{bmatrix} \tag{6}$$

The data have l channels and N samples, such that $[Y]$ has dimensions Nxl. In Cov-SSI, the discrete correlation matrix is an

essential starting point. The discrete correlation matrix at time lag $\Delta t = kf_s^{-1}$ is defined as follows:

$$[R_k] = E\left(\{y_{n+k}\}\{y_n\}^T\right) \tag{7}$$

The discrete cross-correlation matrix is estimated by employing FFT and IFFT transforms, as implemented in the MATLAB function `xcorr`, without normalization.

The correlation matrices are subsequently arranged as submatrices in a block-Hankel matrix, where $2i$ is the maximum number of time lags, as follows:

$$[H_i] = \begin{bmatrix} [R_1] & [R_2] & \dots & [R_i] \\ [R_2] & [R_3] & \dots & [R_{i+1}] \\ \vdots & \vdots & \ddots & \vdots \\ [R_i] & [R_{i+1}] & \dots & [R_{2i+1}] \end{bmatrix} \tag{8}$$

As an alternative to the block-Hankel matrix, a matrix with correlation matrices stacked in a block-Toeplitz manner can be used, as is the case in, e.g. [19]. The following expressions are equally valid for both choices, but the block-Hankel stacking is used in the current paper. The block-Hankel matrix shown in Equation 8 can be decomposed into its observability matrix, $[O_i]$, and controllability matrix, $[C_i]$:

$$[H_i] = [O_i][C_i] \tag{9}$$

which are defined as:

$$[O_i] = \begin{bmatrix} [C] \\ [C][A] \\ [C][A]^2 \\ \vdots \\ [C][A]^{i-1} \end{bmatrix}, \quad [C_i] = \begin{bmatrix} [G] & [A][G] \dots [A]^{i-1}[G] \end{bmatrix} \tag{10}$$

The matrix $[G]$ is the cross-correlation matrix between the one-sample-shifted state vector and the output vector, defined as follows:

$$[G] = E\left(\{z_{n+1}\}\{y_n\}^T\right) \tag{11}$$

The block-Hankel matrix is pre- and post-multiplied with weighting matrices and decomposed using SVD, as follows:

$$\begin{aligned} [W_1][H_i][W_2]^T &= \begin{bmatrix} [U_1] & [U_2] \end{bmatrix} \begin{bmatrix} [\Sigma_1] & [0] \\ [0] & [0] \end{bmatrix} \begin{bmatrix} [V_1]^T \\ [V_2]^T \end{bmatrix} \\ &= [U_1][\Sigma_1][V_1]^T \end{aligned} \tag{12}$$

In practical cases, there will be more non-zero singular values than what is expected for the value of the system order, and thus, input orders have to be specified manually, corresponding to the number of singular values to include in $[\Sigma_1]$. This selection directly affects the resulting eigenvalues and eigenvectors. The selection of an appropriate order is difficult, and therefore, a *stabilization plot* is used to separate physical eigenvalues from spurious ones by estimating the modal parameters for a range of orders. A pole is deemed stable when some criteria for maximum deviance of damping, frequency and mode shape between different values for the system order are fulfilled. This process is described in detail in Section 2.3.

The matrices $[W_1]$ and $[W_2]$ are introduced to improve the identification of poorly excited modes. If the weights are set to identity matrices, this implies no weighting or balanced realisation (BR) weighting. The other weighting considered herein is the canonical variate analysis (CVA) weighting. For a mathematical description of the functioning of the CVA weighting, the reader is referred to [18].

Finally, the state matrix is computed as follows:

$$[A] = [O_{\text{down}}]^{\dagger}[O_{\text{up}}] \tag{13}$$

where $[O_{\text{down}}]$ and $[O_{\text{up}}]$ are obtained by removing the first or last l rows from $[O_i]$, respectively, and $\dagger$ denotes the pseudo-inverse. The output matrix $[C]$ is obtained by extracting the first l rows from $[O_i]$, as follows:

$$[C] = [O_i]_{1:l} \tag{14}$$

The estimated state matrix, $[A]$, then undergoes an eigenvalue decomposition to yield the discrete system poles, $\hat{\lambda}_r$, and system eigenvectors $\{\psi\}$. These are converted to continuous system poles, λ_r, and eigenvectors corresponding to the sensor coordinates, $\{\phi\}$, as follows:

$$\lambda_r = \exp\left(\hat{\lambda}_r f_s^{-1}\right) \tag{15}$$

$$\{\phi\} = [C]\{\psi\} \tag{16}$$

2.2.3. Data-driven stochastic subspace identification

The reader is referred to Van Overschee and de Moor [20] for a comprehensive description of the aspects of the data-driven stochastic subspace identification (Data-SSI) method. For all analyses with the Data-SSI method performed in the current paper, *UPC* weighting is utilized in conjunction with *algorithm 2* [20].

As concluded in the following sections of the paper, the Cov-SSI method is found to be the most robust and accurate method for the purpose of this paper. The mathematical foundation underlying the Data-SSI method is therefore not presented here, and the reader is referred to the cited literature.

2.3. Stabilization criteria and selection of poles

The poles estimated from the SSI algorithms undergo scrutiny from stabilization criteria to assist in distinguishing between physical and spurious modal estimates.

For the order n^*, the resulting poles m^* are compared to all the poles from preceding orders $n = n^* - \sigma$, where $\sigma = 1, 2, \dots, s$ and s is an integer defining the required stability level. The pole m from order n that maximizes the value of a modal indicator, the modal assurance criterion (MAC) number here, is then assumed to correspond to pole m^* in order n^*. The MAC number between complex-valued poles m^* and m is defined as follows [21, 22]:

$$\text{MAC}_{m,m^*} = \frac{|\{\phi_{m^*}\}^T\{\overline{\phi_m}\}|^2}{\{\phi_{m^*}\}^T\{\overline{\phi_{m^*}}\} \cdot \{\phi_m\}^T\{\overline{\phi_m}\}} \tag{17}$$

where $\{\overline{\phi}\}$ corresponds to the complex conjugate of $\{\phi\}$. Most commonly, the natural frequency is used as a modal indicator,

Table 2: Parameters used for the selection of stable poles.

Parameter	Value
Frequency deviance, C_f	1%
Damping deviance, C_ξ	5%
MAC threshold, C_{MAC}	95%
Stability level, s	8

but for cases where the modes are closely spaced in frequency, such as for this case study, the MAC number is considered to be a better choice.

The deviance of certain target quantities between the poles in orders $n = n^* - \sigma$ and the corresponding poles for order n^* are used to check the stability of pole n^* up to the required stability level s by requiring that the following criteria are satisfied:

- $|f_{n^*,m^*} - f_{n,m}|/f_{n^*,m^*} \leq C_f$
- $|\xi_{n^*,m^*} - \xi_{n,m}|/\xi_{n^*,m^*} \leq C_\xi$
- $\text{MAC}\left(\{\phi_{n^*,m^*}\}, \{\phi_{n,m}\}\right) \geq C_{\text{MAC}}$

In the current study, the criterion values and the stability level were selected as indicated in Table 2. Traditionally, the poles deemed as stable are then plotted in a stabilization plot to separate the spurious modes from the physical ones.

3. The Bergsøysund Bridge

The Bergsøysund Bridge is a 931 m long, curved floating bridge that stretches between Aspøya and Bergsøya on the northwestern coast of Norway (see Figure 1). Seven separate light-weight concrete pontoons support the steel superstructure, as is depicted by the photograph in Figure 2. Rubber bearings support the bridge vertically and horizontally at the abutments, and a steel rod on each of the ends absorbs axial forces. No mooring is supporting the bridge, which makes it a particularly interesting case study.

3.1. Structural monitoring system

The monitoring system is described in detail in [23], but the most important details are repeated below for the convenience of the reader. Five anemometers distributed in lampposts on the top of the bridge deck and 6 wave radars distributed close to the centre of the bridge are monitoring the environmental action, while two triaxial accelerometers on each pontoon (14 in total), supplemented with a global navigation satellite system (GNSS) sensor at the centre of the bridge, are monitoring the response of the bridge. The sensor layout is depicted in Figure 3.

4. Analysis

In this section, the modal identification techniques are applied to selected acceleration recordings. There are a total of 6210 recordings made in the time span between November 2014

Figure 1: Map section showing the geography around the bridge site. ©Kartverket.

and January 2017, of which 1679 include sensors for environmental monitoring and all 14 accelerometers. All of these recordings had durations of approximately 30 minutes. The recordings were resampled to 2 Hz after applying a suitable low-pass filter, prior to the identification. Three different characteristics are sought in the pool of recordings to be selected for modal analysis:

1. Low-level response (and excitation)
2. Traffic-induced response
3. Wave-induced response

By investigating these three principally different scenarios, a better understanding of how different loading situations affect the results will hopefully be obtained. Therefore, the starting point was some assessment of the overall statistics of the recordings made to identify such recordings. The wind direction is close to constant at a lateral angle for all three cases. The tools and results presented in Kvåle et al. [23] are used to isolate selected recordings. The traffic indicator (TI) introduced in that work is utilized to indicate the level of traffic proportion of the response, which is defined as follows:

$$\text{TI} = \sqrt{\frac{\sum_{r=1}^{l} \sigma_{\text{hp},r}^2}{\sum_{r=1}^{l} \sigma_r^2}} \tag{18}$$

where σ_r^2 is the variance of channel r and $\sigma_{\text{hp},r}^2$ is the corresponding variance from accelerations high-pass filtered at 2 Hz. Table 3 presents the vital information about the three selected recordings to illustrate the differences between the selected recordings.

Figure 2: The Bergsøysund Bridge. Photograph by NTNU/K.A. Kvåle.

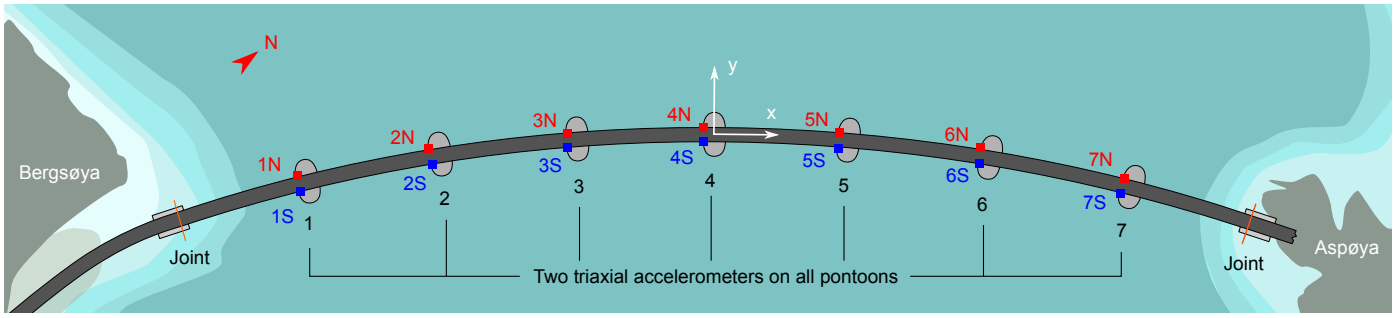

(a) View from the top, including annotation for north direction and the global coordinate system.

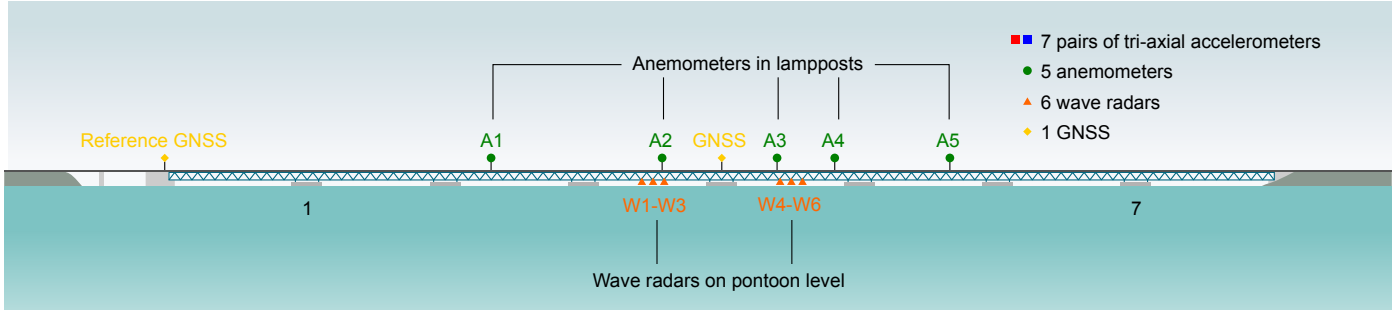

(b) View from the side.

Figure 3: Test set-up on the Bergsøysund Bridge. Reproduced from [23] with permission from Elsevier.

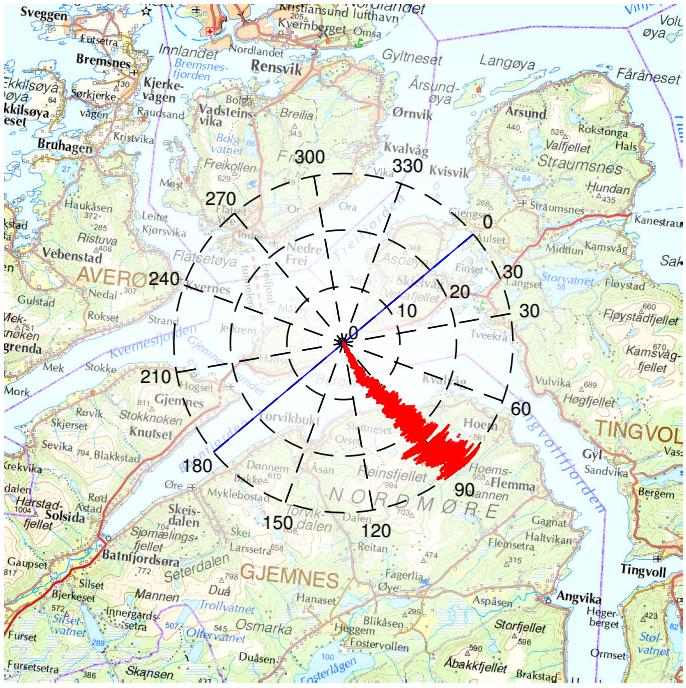

Figure 4: Wind direction time evolution for wave-driven recording. The blue line indicates the tangent at the midspan of the bridge. The plotted wind direction corresponds to the average of anemometers A2 and A3 and indicates the origin of the wind. The amplitude axis corresponds to the time in minutes.

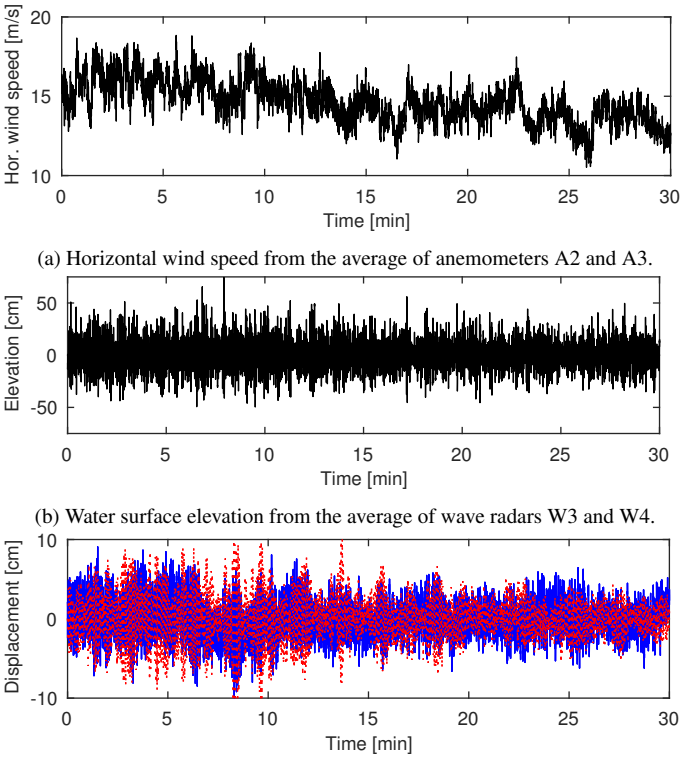

(a) Horizontal wind speed from the average of anemometers A2 and A3.

(b) Water surface elevation from the average of wave radars W3 and W4.

(c) Vertical (solid blue) and lateral (dashed red) displacements of the middle of the bridge obtained from the GNSS sensor.

Figure 5: Time series from the selected wave-driven recording.

The *significant wave height* (SWH) is used as a characteristic measure of the wave height. The SWH is defined as the mean wave height of the highest third of the recorded waves, and it is estimated using the following well-known assumption:

$$H_s = 4\sigma_\eta \tag{19}$$

where σ_η is the standard deviation of the water surface elevation $\eta(t)$. This is valid when the wave height is assumed to be a Gaussian process, which is assumed for all analyses presented in the current paper.

The wind direction of the wave-driven recording is close to perpendicular to the bridge throughout the duration (Figure 4). Figure 5 shows the time histories of the horizontal wind speed, the water surface elevation and the displacements at the midspan of the recording. This figure indicates that the excitation and response recordings are of good quality and that it is sufficiently stationary. The power spectral densities (PSDs) of the lateral acceleration of the midmost pontoon are estimated using Welch's method for assessing the frequency content of the response in the recordings (Figure 6). This figure illustrates that the degree of high-frequency content is much larger in the traffic-driven recording.

4.1. Case-specific identification challenges

The success of a modal identification on the case structure is considered to be challenging due to the following aspects:

- modes are very closely spaced in frequency
- modes have high damping levels
- high degree of influence from external factors

This type of modal analysis therefore requires much from both the identification algorithm and from the operator. The algorithm has to address closely spaced modes, which at the same time have large damping, at least in the context of traditional OMA of civil structures. In addition, a floating bridge will be highly prone to external influences, making the modal parameters dependent on the environmental conditions.

4.2. Identification of modal parameters

The three selected recordings (see Table 3) were used as the basis for modal identification with the following three algorithms: Cov-SSI, Data-SSI, and FDD. The Cov-SSI method outperforms the other two methods in identifying modal parameters from the recording with the wave-driven response (Table 4). Additionally, note that the Cov-SSI algorithm performs better for most recordings with BR weighting, i.e., no weighting, than with CVA weighting. However, the identification of the modal parameters on some recordings is found to benefit from CVA weighting [24]. Data-SSI is found to provide results that are less clear than the Cov-SSI results, including multiple clusters of modes that appear stable with similar mode shapes but different natural frequency and damping estimates. No further efforts are devoted to investigating this result because it is considered beyond the scope. The FDD is not found to be suitable for this application.

Table 3: Thirty-minute statistics of the selected recordings. The reported accelerations are standard deviations. SWH refers to the significant wave height around pontoon 4 based on an average from wave radars W3 and W4, U is the horizontal mean wind speed close to the centre of the bridge based on an average from anemometers A2 and A3, and θ is the direction of origin of the mean wind. All quantities are based on data low-pass filtered at 2 Hz (see [23] for filter specifics). The recording time is reported in local time. TI is used as an abbreviation for the traffic indicator, which indicates the relative high-frequency content of all accelerations.

			Accelerations of pontoon 4, [mg]						
Characteristic	Recording date	Recording time [hh:mm]	Longitudinal (x)	Lateral (y)	Vertical (z)	SWH [cm]	U [m/s]	θ [°]	TI
Low-level response	May 5, 2015	03:14 (GMT+2)	0.01	0.14	0.04	2.0	2.1	109	0.04
Traffic-induced response	May 18, 2015	07:03 (GMT+2)	0.17	0.12	0.31	2.4	1.3	87	0.64
Wave-induced response	December 30, 2015	04:20 (GMT+1)	1.10	7.12	4.26	82.3	14.6	94	0.03

Table 4: Modal parameters identified from the wave-driven recording by manual selection. The following abbreviations are used: H (horizontal), V (vertical), and T (torsional). Note that the analytic values are obtained using the methodology presented in [14] but with an updated model [15].

	Frequency [rad/s]				Damping ratio [%]			MAC (with analytic)		
	Analytic	Cov-SSI	Data-SSI	FDD	Analytic	Cov-SSI	Data-SSI	Cov-SSI	Data-SSI	FDD
1 (H)	0.58	0.59	0.59	0.61	1.63	1.73	1.58	1.00	0.99	0.99
2 (V)	0.99	1.03	-	-	12.25	6.67	-	0.80	-	-
3 (V)	1.03	1.00	-	-	11.24	14.35	-	0.82	-	-
4 (H)	1.05	1.09	-	-	5.00	3.84	-	0.78	-	-
5 (V/H)	1.17	1.22	-	-	7.67	5.43	-	0.92	-	-
6 (H/T)	1.38	-	1.49	-	5.91	-	3.17	-	0.76	-
7 (V)	1.44	1.49	-	-	3.28	2.41	-	0.72	-	-
8 (V)	1.87	-	-	-	1.07	-	-	-	-	-
9 (T/H)	1.95	1.99	-	-	3.62	2.49	-	0.91	-	-
10 (H/T)	2.23	2.31	2.31	-	0.43	2.43	2.17	0.88	0.81	-
11 (T/H)	2.24	-	-	-	3.98	-	-	-	-	-
12 (V)	2.40	2.48	2.48	-	0.35	0.56	0.35	0.92	0.90	-
13 (V)	2.75	2.87	2.86	-	0.29	0.52	0.45	0.74	0.76	-
14 (T/H)	3.10	3.19	3.20	-	0.38	0.90	0.55	0.97	0.89	-
15 (H/T)	3.15	3.03	3.04	3.04	1.29	1.92	1.53	0.97	0.97	0.94
16 (H/T)	3.84	3.63	3.63	3.66	0.72	1.15	1.01	0.99	0.99	0.99
17 (T/H)	4.02	4.17	4.14	4.20	0.29	0.53	0.86	0.98	0.99	0.98
18 (H/T)	4.09	3.86	3.85	3.88	0.59	0.82	0.81	0.99	0.98	0.99
19 (H/T)	5.22	5.40	5.37	5.42	0.35	0.77	0.71	0.99	0.99	0.99
20 (H/T)	6.70	5.78	5.81	-	0.43	0.70	0.76	0.90	0.91	-

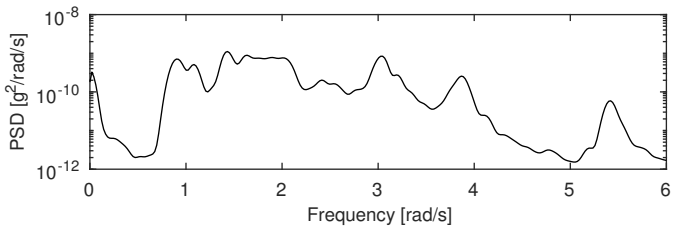

(a) Low-level response.

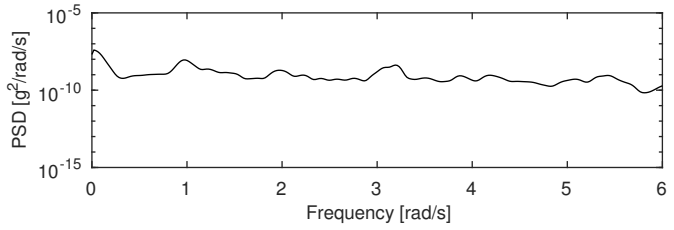

(b) Traffic-induced response.

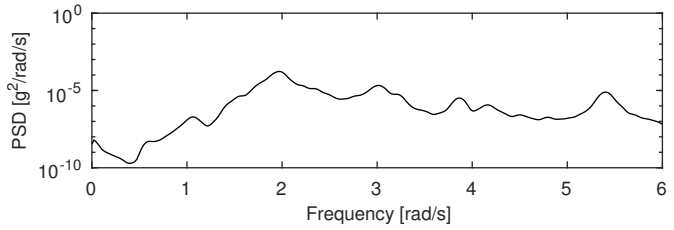

(c) Wave-induced response.

Figure 6: Welch estimates of power spectral densities of the lateral acceleration of the midmost pontoon for the three chosen recordings. Twenty divisions, which are padded by zeros on both sides such that the total length is tripled, are used for the estimates. For reference, the signal-to-noise ratio of the sensor is specified as 130 dB, the dynamic range as 114 dB, and the range as ±4 g.

The mode shapes obtained from the Cov-SSI analysis are presented in Figure 7. The abbreviations H (horizontal), V (vertical), and T (torsional) are used to designate the main displacement patterns of the modes. When combined, the first letter corresponds to the main type of motion. The corresponding Argand phase plots are shown in Figure 8.

Note that the presented mode shapes are in reality snapshots of the mode shapes from the moment where their total real part is at its largest: the mode shapes consist of complex numbers [14], and the components of the mode shapes have phase shifts between them such that they reach their maximum at different time instances. The Argand vectors shown in Figure 8 are rotating with the modal frequency, and their projections along the real axis represent the values of the DOFs. Normally, in modal analysis, it is required that the identified mode shapes have small phase differences, resulting in the modal phase colinearity (MPC) index being close to 1. Because the large added hydrodynamic damping makes the eigenvectors complex, this approach is unsuitable. Moreover, the arc shape of the bridge results in the mode shapes being more coupled in their appearance, including both horizontal, vertical, and torsional motions. The Argand plots shown in Figure 8 reveal that there are significant phase shifts present between the DOFs for single modes. Because the hydrodynamic damping contributions are dependent on the direction, the phase shifts are also prone to be dependent on the motion pattern of the mode under investigation.

For the selected wave-driven recording, the performance of the Cov-SSI method is satisfactory. Most of the first 20 mode shapes from the numerical model are identified, with the only exceptions being modes 6, 8, and 11. Their mode shapes generally have decent MAC values, ranging between 0.72 and 1, and frequency values close to the estimated numerical values. The damping identification is, as expected, the most challenging sub-task. Large variations in the damping ratios are observed (Table 4), with the largest absolute discrepancy observed for mode 2, which is much lower than the predicted value (6.67% versus 12.25%). The critical damping ratio for mode 3, however, is consistently higher than the predicted value (14.35% versus 11.24%). Globally, the damping levels are in agreement with the estimates from the eigenvalue solution of the numerical prediction model.

A manual identification with the Cov-SSI was also performed for the selected low-level and traffic-driven recordings, yielding the results shown in Tables 5 and 6, respectively. Both cases provide below-satisfactory results; in the low-level recording, the bridge is only sufficiently excited to reliably identify 7 of the first 20 modes, whereas the response measurements in the traffic-driven recording results in mode shapes with poor MAC values relative to the numerical predictions.

4.3. On the selection of parameters for the SSI analyses

The results from the SSI analyses are highly dependent on the chosen parameters, and a proper selection of these parameters will therefore vary from application to application. The most important aspects observed in the current case study are presented in the following sub-sections.

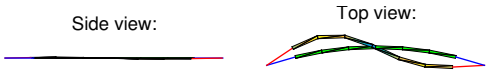

(a) Mode 1 (H). ω_n = 0.59 rad/s, ξ_n = 1.73%, and MAC = 1.00.

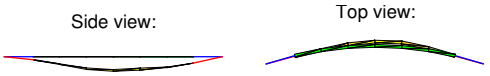

(b) Mode 2 (V). ω_n = 1.03 rad/s, ξ_n = 6.67%, and MAC = 0.80.

(c) Mode 3 (V). ω_n = 1.00 rad/s, ξ_n = 14.35%, and MAC = 0.82.

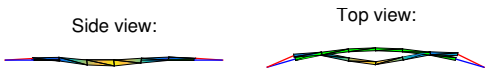

(d) Mode 4 (H). ω_n = 1.09 rad/s, ξ_n = 3.84%, and MAC = 0.78.

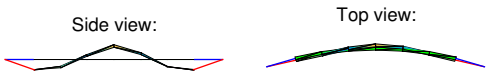

(e) Mode 5 (V/H). ω_n = 1.22 rad/s, ξ_n = 5.43%, and MAC = 0.92.

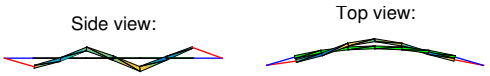

(f) Mode 7 (V). ω_n = 1.49 rad/s, ξ_n = 0.72%, and MAC = 0.72.

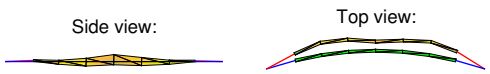

(g) Mode 9 (T/H). ω_n = 1.99 rad/s, ξ_n = 2.49%, and MAC = 0.91.

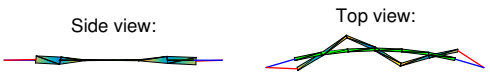

(h) Mode 10 (H/T). ω_n = 2.31 rad/s, ξ_n = 2.43%, and MAC = 0.88.

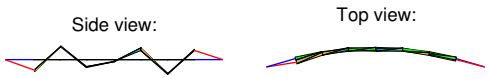

(i) Mode 12 (V). ω_n = 2.48 rad/s, ξ_n = 0.56%, and MAC = 0.92.

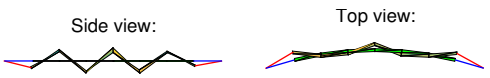

(j) Mode 13 (V). ω_n = 2.87 rad/s, ξ_n = 0.52%, and MAC = 0.74.

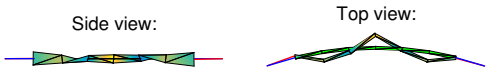

(k) Mode 14 (T/H). ω_n = 3.19 rad/s, ξ_n = 0.90%, and MAC = 0.97.

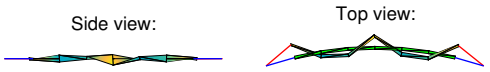

(l) Mode 15 (H/T). ω_n = 3.03 rad/s, ξ_n = 1.92%, and MAC = 0.97.

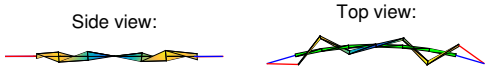

(m) Mode 16 (H/T). ω_n = 3.63 rad/s, ξ_n = 1.15%, and MAC = 0.99.

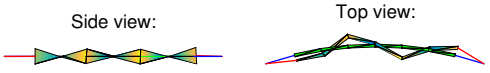

(n) Mode 17 (T/H). ω_n = 4.17 rad/s, ξ_n = 0.53%, and MAC = 0.99.

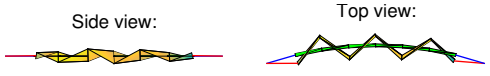

(o) Mode 18 (H/T). ω_n = 3.86 rad/s, ξ_n = 0.82%, and MAC = 0.98.

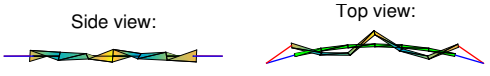

(p) Mode 19 (H/T). ω_n = 5.40 rad/s, ξ_n = 0.77%, and MAC = 0.99.

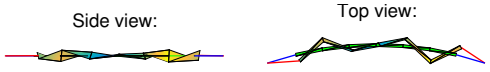

(q) Mode 20 (H/T). ω_n = 5.78 rad/s, ξ_n = 0.70%, and MAC = 0.91.

Figure 7: Identified mode shapes corresponding to the modal parameters shown in Table 4 from the wave-driven recording and using the Cov-SSI method. The following abbreviations are used: H (horizontal), V (vertical), and T (torsional). The numbering refers to the modes obtained from the eigenvalue solution of the numerical prediction model.

Table 5: Modal parameters identified from the low-level recording by manual selection. The following abbreviations are used: H (horizontal), V (vertical), and T (torsional). Note that the analytic values are obtained using the methodology presented in [14] but with an updated model [15].

	Frequency [rad/s]		Damping ratio [%]		
	Analytic	Cov-SSI	Analytic	Cov-SSI	MAC (with analytic)
12 (V)	2.40	2.48	0.35	0.60	0.93
14 (T/H)	3.10	3.18	0.38	0.87	0.94
15 (H/T)	3.15	3.04	1.29	1.40	0.96
16 (H/T)	3.84	3.63	0.72	0.92	0.99
17 (T/H)	4.02	4.16	0.29	0.56	0.99
18 (H/T)	4.09	3.87	0.59	1.03	0.97
19 (H/T)	5.22	5.41	0.35	0.67	0.98

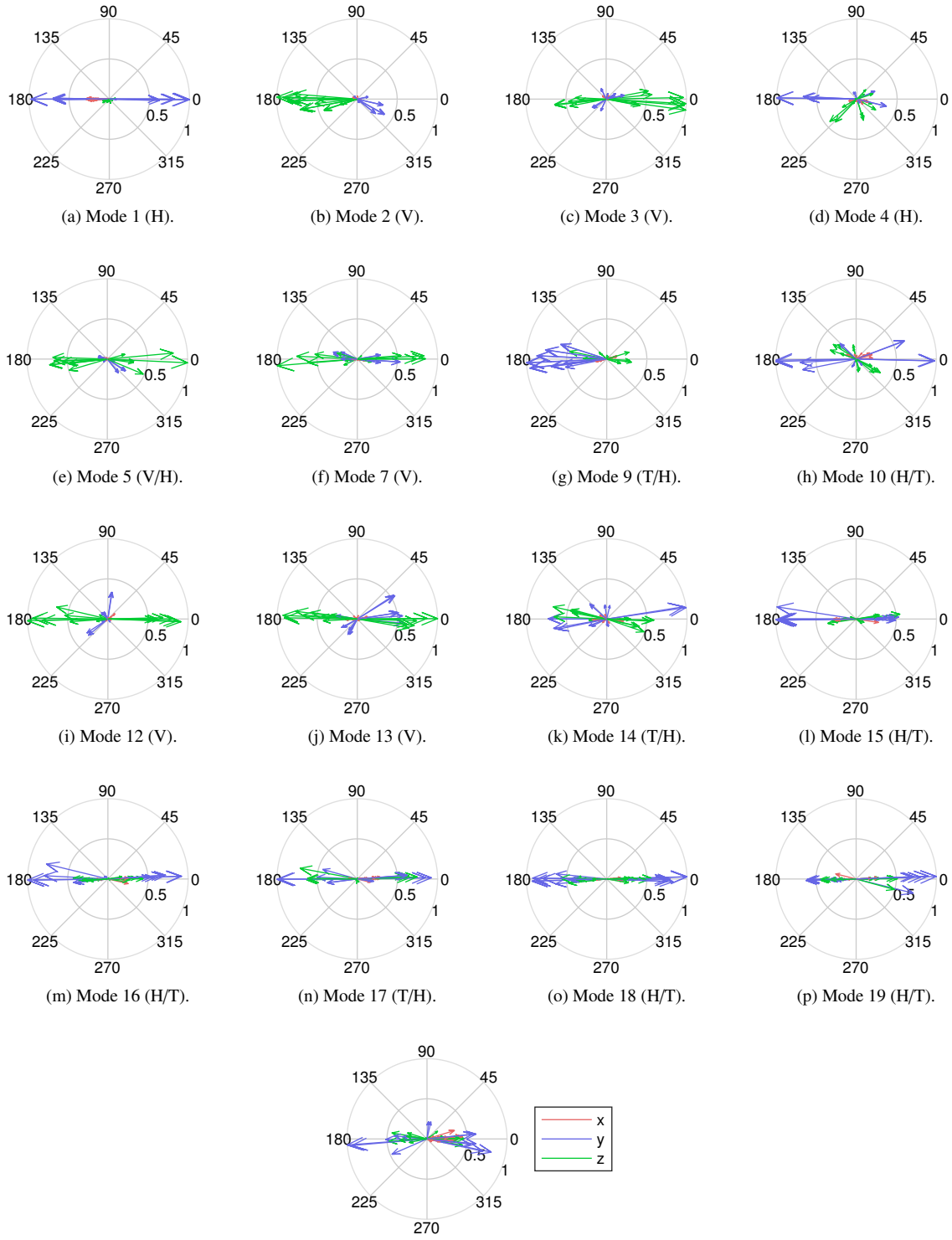

(a) Mode 1 (H). (b) Mode 2 (V). (c) Mode 3 (V). (d) Mode 4 (H).

(e) Mode 5 (V/H). (f) Mode 7 (V). (g) Mode 9 (T/H). (h) Mode 10 (H/T).

(i) Mode 12 (V). (j) Mode 13 (V). (k) Mode 14 (T/H). (l) Mode 15 (H/T).

(m) Mode 16 (H/T). (n) Mode 17 (T/H). (o) Mode 18 (H/T). (p) Mode 19 (H/T).

(q) Mode 20 (H/T) and legend for all plots.

Figure 8: Argand plots of mode shapes corresponding to the modes in Table 4 and Figure 7 from the wave-driven recording and using the Cov-SSI method. The numbering refers to the modes obtained from the eigenvalue solution of the numerical prediction model. All global degrees of freedom (DOFs) originating from all the accelerometer channels are plotted in all plots. The components are presented in different colours depending on whether they are longitudinal (x), lateral (y) or vertical (z).

Table 6: Modal parameters identified from the traffic-driven recording by manual selection. The following abbreviations are used: H (horizontal), V (vertical), and T (torsional). Note that the analytic values are obtained using the methodology presented in [14] but with an updated model [15].

	Frequency [rad/s]		Damping ratio [%]		
	Analytic	Cov-SSI	Analytic	Cov-SSI	MAC (with analytic)
4 (H)	1.05	0.97	5.00	2.92	0.47
7 (V)	1.44	1.48	3.28	1.90	0.88
8 (V)	1.87	1.94	1.07	0.91	0.84
11 (T/H)	2.24	2.26	3.98	0.73	0.57
12 (V)	2.40	2.49	0.35	0.38	0.98
13 (V)	2.75	2.87	0.29	0.64	0.68
14 (T/H)	3.10	3.19	0.38	0.62	0.81
15 (H/T)	3.15	3.07	1.29	0.76	0.39
17 (T/H)	4.02	4.16	0.29	0.46	0.63
18 (H/T)	4.09	3.88	0.59	0.80	0.50

4.3.1. Duration

The durations of the recordings were kept fixed at approximately 30 minutes. For practical reasons, when subdividing long recordings, the duration was allowed to range between 29 and 30 minutes, i.e., $T \in [29\text{min}, 30\text{min}]$. For a structure that is heavily influenced by a single environmental process, it is not beneficial with a very long recording, contrary to the case for structures less controlled by a single process. The stationarity of the process, and thus the response of the structure, is an important concern. The durations of the recordings are therefore a compromise between keeping the recordings near stationary while simultaneously increasing the durations to acceptable levels. The optimum length will be dependent on the level of non-stationarity of the loading process. No stationarity checks were conducted in the following study. However, visual inspections of the recorded time histories were performed to ensure that no abrupt changes occurred in the excitation or response.

4.3.2. Blockrows

The number of blockrows is the main input parameter of SSI analyses, and its selection affects the solution to a large extent. The number of blockrows should be chosen to be large enough such that the time lags represented in the covariance matrix have sufficient length to be able to describe the lowest frequencies of interest in the data. If the number of chosen blockrows is too low, these components will simply not be identified with confidence. If the number of chosen blockrows is too high, the amount of spurious modes will increase. For the wave-driven recording, $i = 24$, corresponding to a maximum time lag of $\tau = 2 \cdot 24 \cdot 2^{-1} = 24$ seconds or a minimum frequency of $f = \frac{1}{24} \approx 0.04Hz$, was found to be a good compromise between clear stabilization plots and the number of modes visible for various stability levels (Figure 9). The sample rate, which was 2 Hz in the current application, is a critical quantity to consider together with the number of blockrows. The effects that changes of blockrows have on the modal parameters are not considered in the current paper.

4.3.3. Stabilization level

The selection of the stabilization level in the plotting of the stabilization plots is powerful for tweaking the results. A low

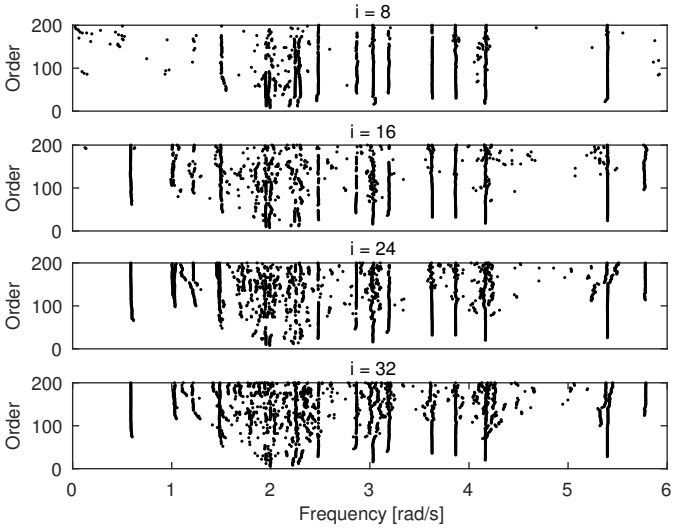

(a) Stability level, $s = 2$.

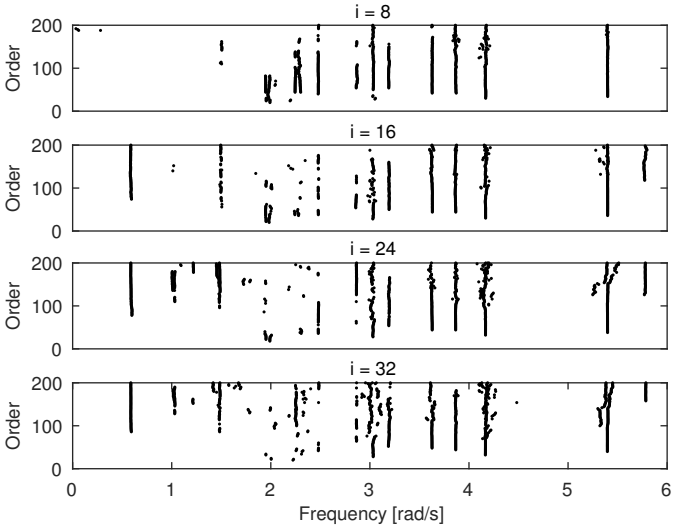

(b) Stability level, $s = 8$.

Figure 9: Stabilization plots with different blockrows, i, for Cov-SSI analyses of the wave-driven recording.

stabilization level in combination with a high number of blockrows results in a very cluttered stabilization plot, which is a difficult starting point for separating the physical poles from the spurious ones (Figure 10). Thus, the stability level should be selected with consideration of the blockrows. In the following, a stability level of $s = 8$ is found to be suitable in combination with $i = 24$. The clutter in the stabilization plots for the three cases, shown in Figure 10, is located at different frequencies. By comparing with the spectral densities of the lateral accelerations of the midmost pontoon, estimated using Welch's method and plotted in Figure 6, there is a striking resemblance: the loading processes acting on the structure differing from a white noise process result in false poles, which are only identified as unstable when the stability level is increased.

4.3.4. Orders

The maximum of the range of orders is simply selected based on visual inspection of the stabilization plot, with the requirement that no new straightly aligned (stable) poles are developed for increasing order. A reasonable selection of orders, based on the other parameters set above and visual inspection of the stabilization plots, is $n = 2, 4, \ldots, 200$.

4.4. Environmental influence and automatic OMA

By automating the selection of modal parameters from each recording, the effects of weather and environment on the modal parameters can be investigated. The eigenvalue solution of the numerical prediction model was used as a reference to ensure a consistent numbering of the identified modes. Due to the combination of efficiency and accuracy of the Cov-SSI method, this was selected for the automatic OMA. The Cov-SSI parameters for all analyses were set according to the findings in the preceding section ($i = 24$, $s = 8$, $T \in [29\text{min}, 30\text{min}]$, and $n = 2, 4, \ldots, 200$). First, the stabilization criteria have to be fulfilled, as described in Section 2.3. Second, the MAC values between the poles and the modes from the eigenvalue solution have to be above a predefined value MAC_{ref} for them to be considered. The pole with the largest MAC value with the corresponding mode from the numerical prediction model is used as a reference, and all modes within certain slacks in frequency (S_f), damping (S_ξ) and MAC (S_{MAC}) from this are chosen. Finally, the means and standard deviations of all the chosen frequencies, damping ratios and MACs are calculated. The allowed slack and the required MAC value are presented in Table 8. The presented values were used for the entire period under investigation. Figure 11 shows the resulting identified modes overlaid on the stabilization plots for the three selected recordings. This figure is supported by the numerical data in Table 7. The automatic algorithm works well for the wave-driven recording and performs decently for the low-level response recording. The selected traffic-driven recording performs poorly and appears to contain spurious modes from harmonics at multiple frequencies, represented by several scattered poles in Figure 11b. The only reason that these are not erroneously interpreted as modes is because the predicted mode shapes, obtained from the eigenvalue solution of the numerical

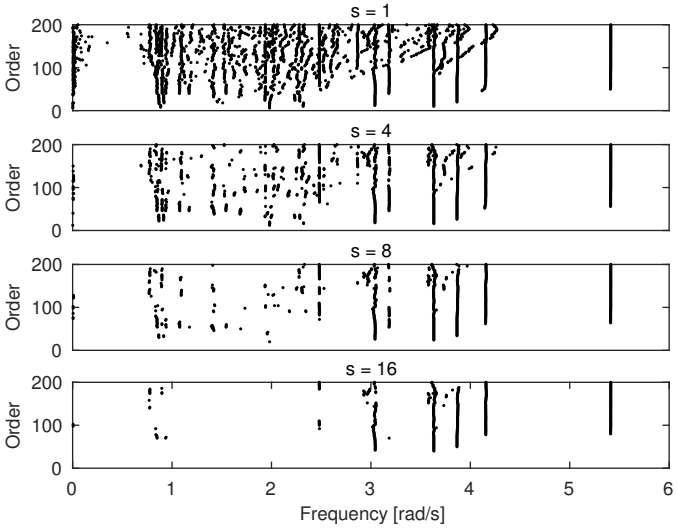

(a) Low-level recording.

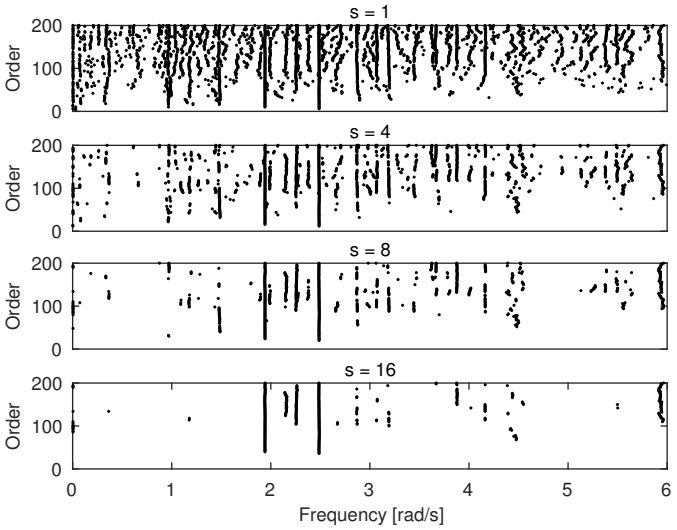

(b) Traffic-driven recording.

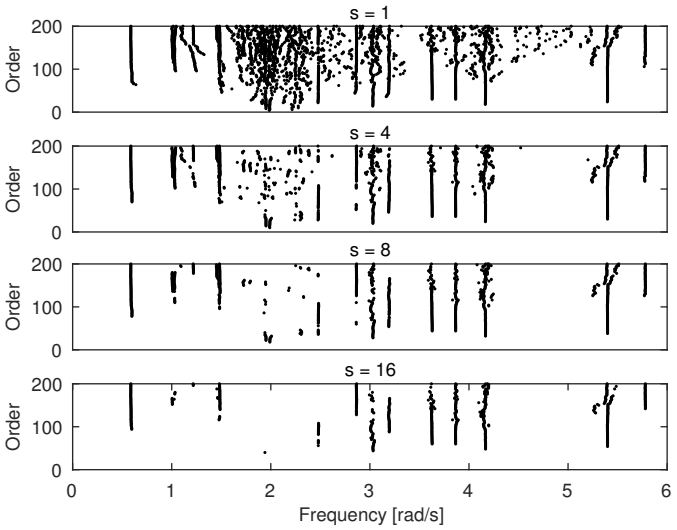

(c) Wave-driven recording.

Figure 10: Stabilization plots with different stability levels, s, for Cov-SSI analyses with blockrows, $i = 24$.

Table 7: Automatically identified modes from the wave-driven recording. Three standard deviations are used as the measure for accuracy. *Damping* refers to the critical damping ratio [%], while *frequency* refers to the undamped natural frequency [rad/s]. The following abbreviations are used: H (horizontal), V (vertical), and T (torsional).

	Analytic		Cov-SSI		
Mode	Frequency	Damping	Frequency	Damping	MAC
1 (H)	0.58	1.63	0.59 ± 0.00	1.9 ± 0.56	0.99 ± 0.00
2 (V)	0.99	12.25	1.03 ± 0.01	6.5 ± 0.50	0.76 ± 0.13
3 (V)	1.03	11.24	1.01 ± 0.01	14.5 ± 1.08	0.84 ± 0.05
4 (H)	1.05	5.00	1.09 ± 0.01	3.8 ± 0.31	0.78 ± 0.02
5 (V/H)	1.17	7.67	1.22 ± 0.00	5.5 ± 0.37	0.92 ± 0.01
6 (H/T)	1.38	5.91	1.45 ± 0.00	6.5 ± 0.47	0.71 ± 0.01
7 (V)	1.44	3.28	1.48 ± 0.01	2.3 ± 0.27	0.71 ± 0.02
8 (V)	1.87	1.07	-	-	-
9 (T/H)	1.95	3.62	1.99 ± 0.02	2.4 ± 0.56	0.90 ± 0.05
10 (H/T)	2.23	0.43	2.31 ± 0.04	2.7 ± 1.39	0.88 ± 0.18
11 (T/H)	2.24	3.98	-	-	-
12 (V)	2.40	0.35	2.48 ± 0.00	0.6 ± 0.06	0.91 ± 0.06
13 (V)	2.75	0.29	2.86 ± 0.00	0.5 ± 0.13	0.75 ± 0.07
14 (T/H)	3.10	0.38	3.19 ± 0.01	0.9 ± 0.33	0.97 ± 0.02
15 (H/T)	3.15	1.29	3.03 ± 0.03	2.1 ± 1.29	0.96 ± 0.04
16 (H/T)	3.84	0.72	3.62 ± 0.02	1.1 ± 0.58	0.98 ± 0.02
17 (T/H)	4.02	0.29	4.17 ± 0.08	0.6 ± 0.52	0.98 ± 0.03
18 (H/T)	4.09	0.59	3.87 ± 0.02	0.8 ± 0.41	0.98 ± 0.01
19 (H/T)	5.22	0.35	5.40 ± 0.13	0.7 ± 0.34	0.98 ± 0.04
20 (H/T)	6.70	0.43	5.78 ± 0.01	0.9 ± 0.36	0.91 ± 0.03

Table 8: Slack allowance and MAC requirement (to analytical modes).

Parameter	Value
Frequency slack, S_f	10%
Damping slack, S_ξ	50%
MAC slack, S_{MAC}	10%
MAC requirement, $\mathrm{MAC}_{\mathrm{ref}}$	0.7

prediction model, are used as a reference. Our general preference has been placed on the quality rather than the quantity of the data; thus, both data and modal results suspected of being of poor quality are rejected automatically. The disadvantage is that the number of data points for statistical analyses may be smaller than preferred.

The procedure is dependent on a well-tuned numerical prediction model, and it will not handle changes in mode shape very well. Furthermore, for higher modes, the number of accelerometers installed will not be sufficient to capture the motion between the pontoons, and the MAC numbers will erroneously tend to large values. However, the authors believe that the simple procedure presented herein will capture the main aspects of the bridge's behaviour in a robust manner.

The averaged identified damping estimates from all recordings are illustrated for the first 20 modes in Figure 12. The error bars indicate one standard deviation above and below the mean value.

Figure 13 shows the *coefficient of variation* of the natural frequency, $C_{v,\omega}$, and damping ratio, $C_{v,\xi}$, for the first 20 modes. The coefficient of variation is defined as the mean-normalized standard deviation, i.e., $C_v = \sigma/\mu$. The figure reveals a decent level of variation in the identified natural frequencies. It also reveals that there are large variations in the identified damping ratios, as expected. Some modes are only identified in a small selection of the pool of recordings, resulting in a very low number of samples and thus a poor starting point for estimating statistical derivatives.

The identified natural frequencies and damping ratios for the first six modes are illustrated in Figure 14. This figure reveals a clear reduction in scatter for increased excitation levels, represented by SWH here. This effect is believed to primarily arise from the uncertainty in the identification, which is far larger for small excitation levels. The reduced excitation levels also result in the fact that the uncertain and unaccounted excitation sources, such as traffic, accounts for far more of the total load and consequently increases the scatter. The damping levels show an increasing tendency to increasing excitation levels, which is reasonable. A similar study was performed on the effect of changing wind speeds. The results of that study were very similar but more scattered. This difference is explained by the fact that the wind controls the waves, but the bridge response and hence the modal analysis results are primarily affected by the waves. Consequently, no such results are reported herein. The effect of changes in the tidal levels, which normally vary by approximately 2 m on site, on the modal parameters was found to be insignificant. No relation between the traffic level, characterized by the TI, and the damping level was visible. Note that no rejection criterion based on the stationarity level is applied and that non-stationarity in the recordings might cause more scatter.

5. Concluding remarks

Based on recordings from the state-of-the-art monitoring system installed on the Bergsøysund Bridge, measuring both response (accelerations and displacements) and environmental actions (wind and waves), system identification has been successfully performed on the acceleration recordings and are interpreted in light of the recorded environmental factors. The Cov-SSI, Data-SSI and FDD methods have been applied for manual identification surveys, and the resulting identified modes have been compared with the modal quantities obtained from the solution of the eigenvalue problem from a comprehensive numerical model set-up. The Cov-SSI method shows the most promise among the methods. The Data-SSI method also provides decent results, whereas the FDD method is insufficient for this application. Natural frequencies and mode shapes are very well identified, whereas there are relatively large uncertainties in the identification of the damping ratios. However, the overall damping levels are consistent with the estimates from the eigenvalue solution of the numerical prediction model. Large damping levels, closely spaced modes, and a geometric design resulting in coupled motion make the identification procedure challenging. Due to scattered stabilization plots, the interpretation and manual selection are tasks that add additional uncertainties to the results.

Due to the complexity of the problem, effort has to be placed on the selection of the analysis parameters. The number of blockrows is a parameter that directly affects the results of the algorithm, and it should be chosen with care. By producing stabilization plots with different numbers of blockrows, a reasonable value was chosen based on visual inspection of the plots.

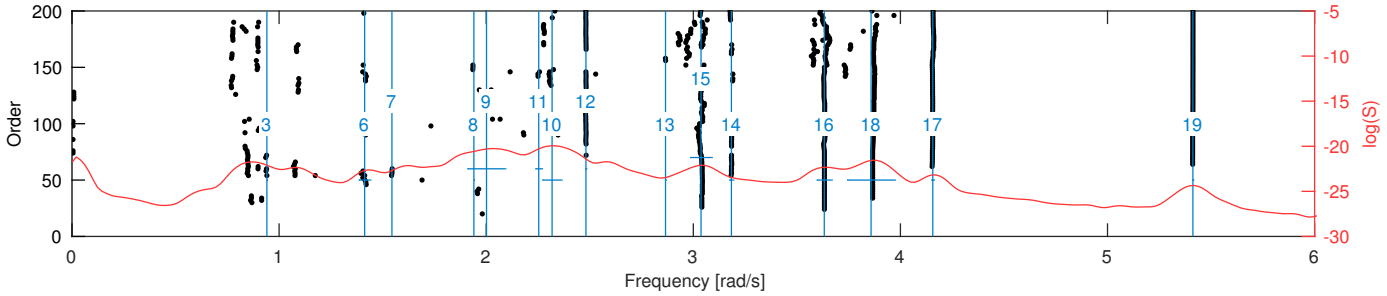

(a) Low-level response.

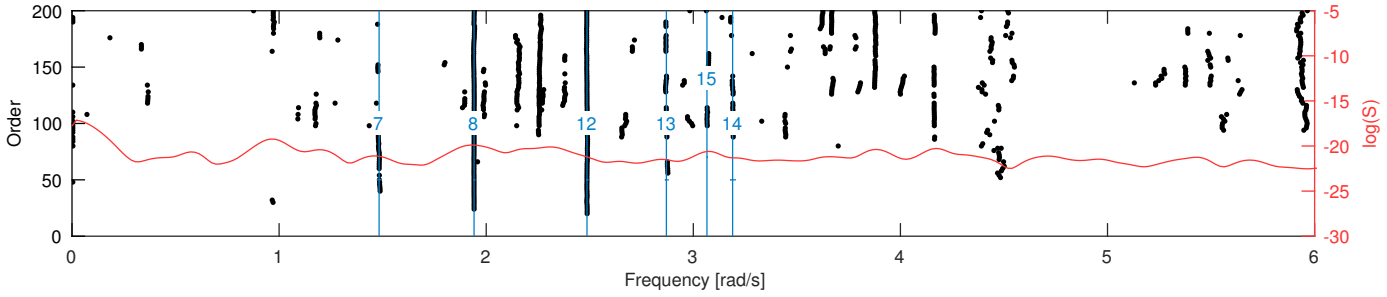

(b) Traffic-induced response.

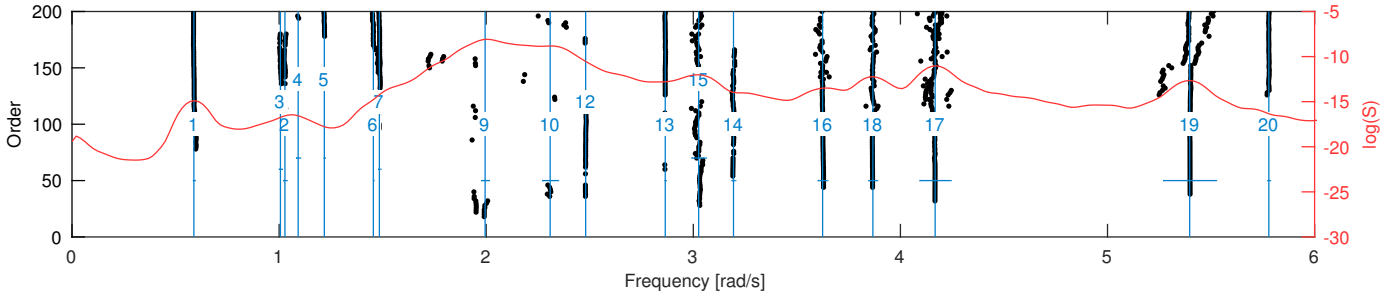

(c) Wave-induced response.

Figure 11: Stabilization plots for the automatic Cov-SSI analyses of the three selected recordings. Only the poles deemed stable are shown here, in agreement with the requirements stated in Table 2. Vertical lines indicate the modes identified, and horizontal lines denote $\pm 3\sigma_\omega$, corresponding to the stable poles within the predefined slack and above the MAC requirement presented in Table 8. The numbers refer to the numbers of analytical modes. The red lines show the power spectral density estimate from the lateral acceleration of pontoon 3, corresponding to the indicated recording.

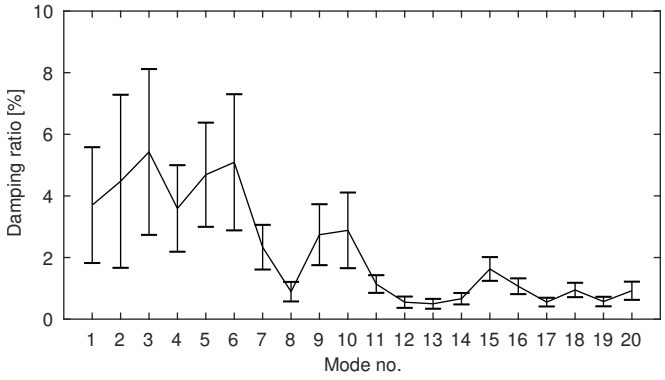

Figure 12: Average estimated damping ratios for the first 20 modes. The error bars represent one standard deviation ($\pm\sigma$).

To reduce clutter in the stabilization plots, a rather large stabilization level is recommended. A stabilization level of $s = 8$ was utilized, with a good result, in the current paper.

By automating the selection of stable poles, relying on the mode shapes from the eigenvalue solution of the numerical prediction model, a study on the effect of the wave excitation on the natural frequency and damping was performed. This study revealed that the uncertainties in the identified modal quantities are generally reduced when the excitation level increases. This is believed to be a consequence of a larger proportion of the excitation being known, as well as the identification algorithms performing better for larger response levels. Furthermore, the damping levels tend to increase for increasing SWH.

5.1. Future work

The selection of the system identification technique is a difficult task, and other methods should also be considered for the task. In particular, methods better suited for problems with loading processes that considerably differ from white noise, such as blind source separation (BSS) methods, should be considered. Furthermore, more sophisticated techniques for the automatic selection of poles should be applied. This may enable stronger conclusions about the effect from the environmental parameters to be drawn.

ACKNOWLEDGEMENTS

This research was conducted with financial support from the Norwegian Public Roads Administration. The authors gratefully acknowledge this support.

REFERENCES

[1] E. Watanabe, T. Utsunomiya, Analysis and design of floating bridges, Progress in Structural Engineering and Materials 5 (3) (2003) 127–144. doi:10.1002/pse.151.
URL http://dx.doi.org/10.1002/pse.151

[2] V. R. McLamore, G. C. Hart, I. R. Stubbs, Ambient vibration of two suspension bridges, Journal of the Structural Division 97 (10) (1971) 2567–2582.

[3] J. M. W. Brownjohn, F. Magalhaes, E. Caetano, A. Cunha, Ambient vibration re-testing and operational modal analysis of the Humber Bridge, Engineering Structures 32 (8) (2010) 2003–2018. doi:10.1016/j.engstruct.2010.02.034.
URL http://linkinghub.elsevier.com/retrieve/pii/S0141029610000878

[4] B. Peeters, G. De Roeck, One-year monitoring of the Z24-Bridge: environmental effects versus damage events, Earthquake Engineering & Structural Dynamics 30 (2) (2001) 149–171. doi:10.1002/1096-9845(200102)30:2<149::AID-EQE1>3.0.CO;2-Z.

[5] C. Farrar, G. James, SYSTEM IDENTIFICATION FROM AMBIENT VIBRATION MEASUREMENTS ON A BRIDGE, Journal of Sound and Vibration 205 (1) (1997) 1–18. doi:10.1006/jsvi.1997.0977.
URL http://www.sciencedirect.com/science/article/pii/S0022460X97909779

[6] F. Magalhães, Á. Cunha, E. Caetano, Dynamic monitoring of a long span arch bridge, Engineering Structures 30 (11) (2008) 3034–3044. doi:10.1016/j.engstruct.2008.04.020.
URL http://www.sciencedirect.com/science/article/pii/S0141029608001405

[7] J. M. W. Brownjohn, P. Moyo, P. Omenzetter, Y. Lu, Assessment of Highway Bridge Upgrading by Dynamic Testing and Finite-Element Model Updating, Journal of Bridge Engineering 8 (3) (2003) 162–172. doi:10.1061/(ASCE)1084-0702(2003)8:3(162).
URL http://dx.doi.org/10.1061/(ASCE)1084-0702(2003)8:3(162)

[8] P. Andersen, R. Brincker, B. Peeters, G. De Roeck, L. Hermans, C. Krämer, Comparison of system identification methods using ambient bridge test data, in: Proc. of the 17th International Modal Analysis Conference, Kissimee, Florida, 1999, pp. 7–10.

[9] B. Peeters, C. Ventura, Comparative study of modal analysis techniques for bridge dynamic characteristics, Mechanical Systems and Signal Processing 17 (2003) 965–988. doi:10.1006/mssp.2002.1568.
URL http://www.sciencedirect.com/science/article/pii/S0888327002915682

[10] J. M. W. Brownjohn, E. P. Carden, Tracking the effects of changing environmental conditions on the modal parameters of Tamar Bridge, in: 3rd international conference on structural health monitoring and intelligent infrastructure, 2007.

[11] A. Cabboi, F. Magalhães, C. Gentile, Á. Cunha, Automated modal identification and tracking: Application to an iron arch bridge, Structural Control and Health Monitoringdoi:10.1002/stc.1854.
URL http://dx.doi.org/10.1002/stc.1854

[12] K. A. Kvåle, O. Øiseth, A. Rønnquist, R. Sigbjörnsson, Modal Analysis of a Floating Bridge Without Side-Mooring, in: Dynamics of Civil Structures, Volume 2, Vol. 2, Springer, 2015, pp. 127–136. doi:10.1007/978-3-319-15248-6_14.
URL http://link.springer.com/10.1007/978-3-319-15248-6{_}14

[13] C. Rainieri, G. Fabbrocino, E. Cosenza, Some remarks on experimental estimation of damping for seismic design of civil constructions, Shock and Vibration 17 (4, 5) (2010) 383–395.

[14] K. A. Kvåle, R. Sigbjörnsson, O. Øiseth, Modelling the stochastic dynamic behaviour of a pontoon bridge: A case study, Computers & Structures 165 (2016) 123–135. doi:10.1016/j.compstruc.2015.12.009.
URL http://linkinghub.elsevier.com/retrieve/pii/S004579491500334X

[15] Ø. W. Petersen, O. Øiseth, Sensitivity-based finite element model updating of a pontoon bridge, Submitted to Engineering Structures.

[16] R. Brincker, L. Zhang, P. Andersen, Modal Identication from Ambient Responses using Frequency Domain Decomposition, in: Proceedings of 18th International Modal Analysis Conference, 2000, pp. 625–630.

[17] R. Brincker, L. Zhang, P. Andersen, Modal identification of output-only systems using frequency domain decomposition, Smart materials and structures 10 (3) (2001) 441.

[18] L. HERMANS, H. VAN DER AUWERAER, MODAL TESTING AND ANALYSIS OF STRUCTURES UNDER OPERATIONAL CONDITIONS: INDUSTRIAL APPLICATIONS, Mechanical Systems and Signal Processing 13 (2) (1999) 193–216. doi:http://dx.doi.org/10.1006/mssp.1998.1211.

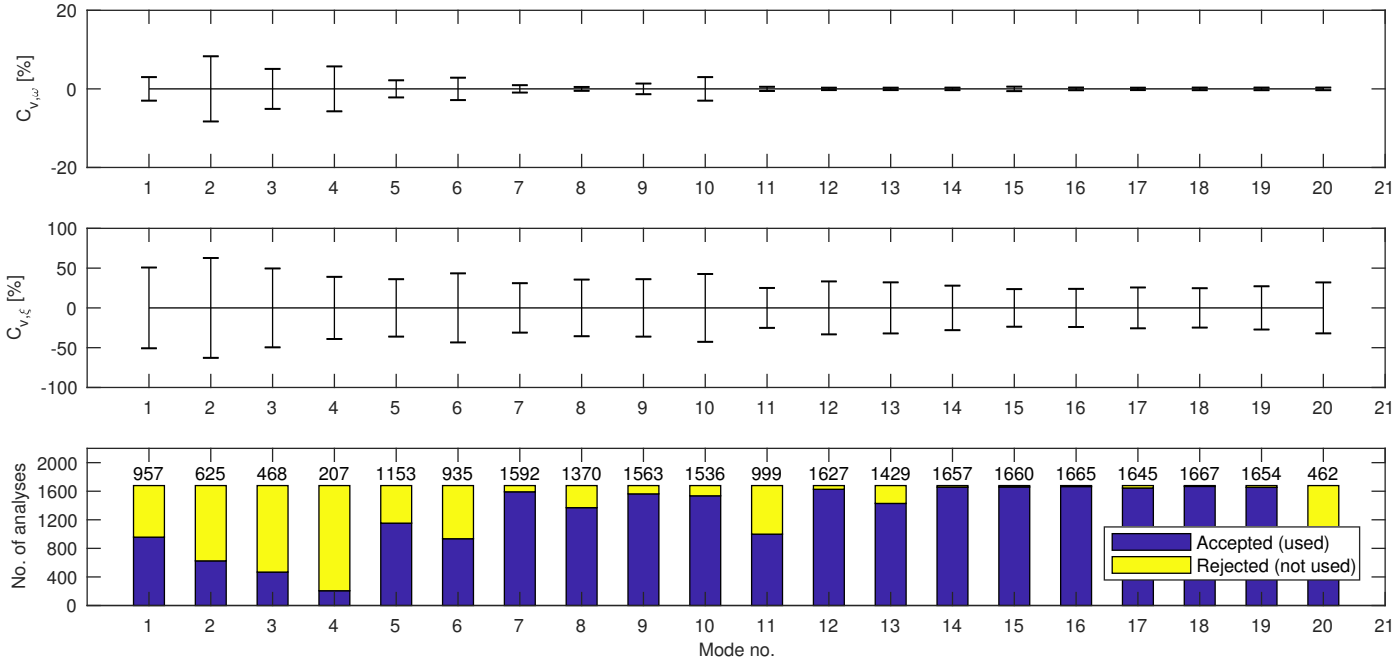

Figure 13: Coefficient of variation of natural frequency and damping ratio for the first 20 modes. The numbers on top of the bars represent the number of accepted analyses, i.e., the number of samples used for the estimate of the coefficient of variation.

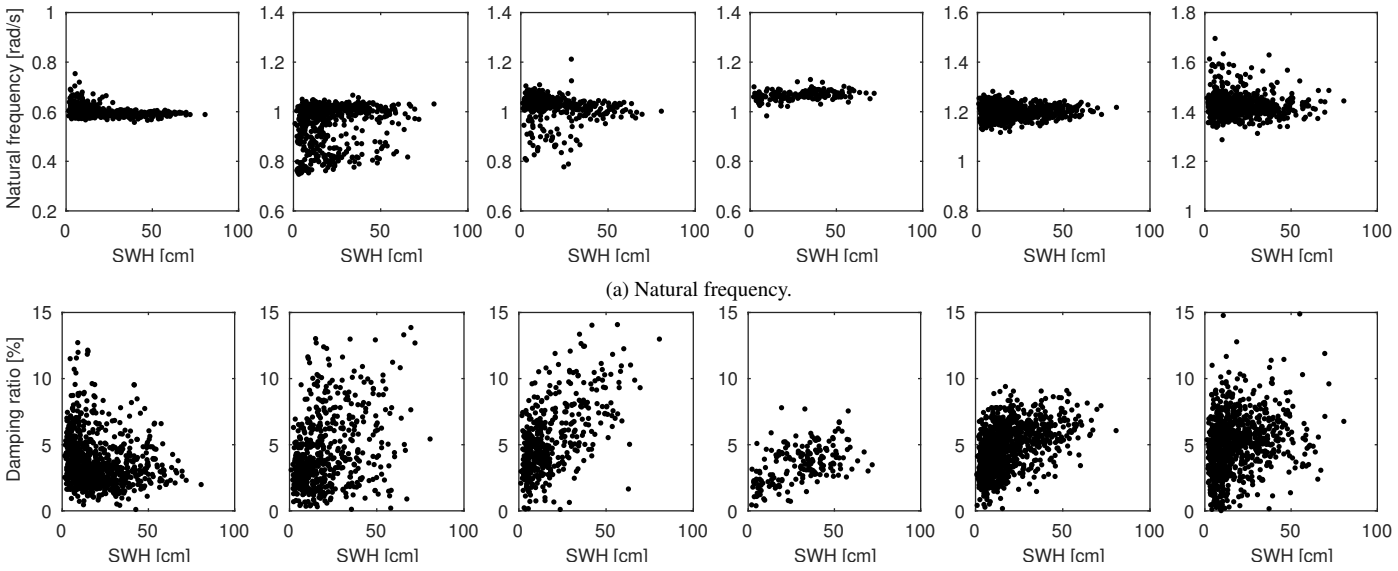

(a) Natural frequency.

(b) Damping ratio.

Figure 14: The effect of the SWH on the identified modal parameters, arranged ascending from mode 1 to mode 6 (left to right).

URL http://www.sciencedirect.com/science/article/pii/S0888327098912110

[19] C. Rainieri, G. Fabbrocino, Operational Modal Analysis of Civil Engineering Structures, Springer, New York, 2014.

[20] P. Van Overschee, B. De Moor, Subspace identification for linear systems: theory, implementation, applications, Kluwer Academic Publishers, Boston/London/Dordrecht, 1996.

[21] R. J. Allemang, D. L. Brown, A correlation coefficient for modal vector analysis, in: Proceedings of the 1st international modal analysis conference, Vol. 1, SEM, Orlando, 1982, pp. 110–116.

[22] R. J. Allemang, The modal assurance criteriontwenty years of use and abuse, Sound and vibration 37 (8) (2003) 14–23.

[23] K. A. Kvåle, O. Øiseth, Structural monitoring of an end-supported pontoon bridge, Marine Structures 52 (2017) 188–207. doi:10.1016/j.marstruc.2016.12.004.
URL http://linkinghub.elsevier.com/retrieve/pii/S0951833916300284

[24] K. A. Kvåle, O. Øiseth, A. Rönnquist, Covariance-Driven Stochastic Subspace Identification of an End-Supported Pontoon Bridge Under Varying Environmental Conditions, in: J. Caicedo, S. Pakzad (Eds.), Dynamics of Civil Structures, Volume 2. Conference Proceedings of the Society for Experimental Mechanics Series., Springer International Publishing, Cham, 2017, pp. 107–115. doi:10.1007/978-3-319-54777-0_14.
URL http://dx.doi.org/10.1007/978-3-319-54777-0{_}14